

Ground-Based Coronagraphy with High Order Adaptive Optics

Anand Sivaramakrishnan

*Space Telescope Science Institute
3700 San Martin Drive, Baltimore, MD 21218*

anands@stsci.edu

Christopher D. Koresko¹

*Division of Geology and Planetary Sciences
California Institute of Technology, Pasadena CA 91125*

Russell B. Makidon

*Space Telescope Science Institute
3700 San Martin Drive, Baltimore, MD 21218*

Thomas Berkefeld²

*Max-Planck Institut fur Astronomie
Königstuhl 17, D-69117 Heidelberg, Germany*

and

Marc J. Kuchner³

*Palomar Observatory
California Institute of Technology, Pasadena CA 91125*

ABSTRACT

We summarize the theory of coronagraphic optics, and identify a dimensionless fine-tuning parameter, \mathcal{F} , which we use to describe the Lyot stop size in the natural units of the coronagraphic optical train and the observing wavelength. We then present simulations of coronagraphs matched to adaptive optics (AO) systems on the Calypso

¹Current address: Jet Propulsion Laboratory, 4800 Oak Grove Drive, Pasadena CA 91109

²Current address: Kiepenheuer - Institut fur Sonnenphysik, Schöneckstrasse 6, D - 79104 Freiburg, Germany

³Current address: Harvard-Smithsonian Center for Astrophysics, Mail Stop 20 60 Garden Street, Cambridge, MA 02138

1.2m, Palomar Hale 5m and Gemini 8m telescopes under various atmospheric conditions, and identify useful parameter ranges for *AO* coronagraphy on these telescopes. Our simulations employ a tapered, high-pass filter in spatial frequency space to mimic the action of adaptive wavefront correction. We test the validity of this representation of *AO* correction by comparing our simulations with recent *K*-band data from the 241-channel Palomar Hale *AO* system and its dedicated PHARO science camera in coronagraphic mode. Our choice of monochromatic modeling enables us to distinguish between underlying halo suppression and bright Airy ring suppression in the final coronagraphic images. For a given telescope–*AO* system combination, we find that *AO* systems delivering images with Strehl ratios below a threshold value are not well-suited to diffraction-limited coronagraphs. When Strehl ratios are above this threshold, an optimized coronagraph with occulting image plane stops as small as $4\lambda/D$ create a region around the *AO* target where dynamic range is significantly enhanced.

Subject headings: instruments: coronagraphs – instruments: miscellaneous – techniques: coronagraphy

1. Introduction

Many ground-based telescopes use adaptive optics (*AO*) to produce diffraction-limited images at near-infrared and visible wavelengths. The point spread function (*PSF*) of a telescope using *AO* typically consists of a bright, diffraction-limited core with several Airy rings superimposed on a wide scattered light halo containing several percent of the total flux. The improvement in image quality that *AO* provides makes it possible to study the region within a few times the diffraction width of the image of a bright star, with dynamic range limited by the presence of the halo and bright Airy rings rather than by atmospheric seeing.

Present-day astronomical *AO* systems routinely deliver Strehl ratios of 30–70% (the Strehl ratio is the ratio of the peak intensity of the image to the peak intensity of the image if the wavefront were free of all aberration). In this paper we look at what is possible when optimized coronagraphs are used with *AO* systems delivering 50–95% Strehl ratios. We believe that this should be the next scientifically-driven step for traditional *AO* systems, since the instruments we model here will open up a new range of ground-based astronomical investigation, and provide a stepping stone to even higher dynamic range ground-based astronomy that is outside the reach of multi-conjugate *AO* systems used to correct wide fields of view (Berkefeld et al. 2001a).

A coronagraph used in conjunction with an *AO* system can improve the sensitivity of an imaging system to faint structure surrounding a bright source. This device blocks the core of the image of an on-axis point source and suppresses the bright diffraction rings and halo, removing light which would otherwise reduce the dynamic range of the imaging. This enables faint off-axis structure to be observed.

Initial observational investigation of the dynamic range achievable with a coronagraph on the Palomar Hale 5m *AO* system has demonstrated the importance of understanding the interaction between the *AO* system and coronagraphic instrument parameters (Oppenheimer et al. 2000). The choice of pupil plane and image plane stops sizes can only be made by understanding image formation by the *AO* system and the interaction between the *AO* system and the coronagraph. A traditional coronagraph reduces off-axis light from an on-axis source with two optical stops: an occulting stop in the image plane, and a matched Lyot stop in the next pupil plane. An alternative solution to this problem is a nulling coronagraph (*e.g.*, Guyon et al. (1999)), although this novel approach still needs technological development in order to be applied to broad-band imaging. The discovery space of a nulling coronagraph is also somewhat complementary to the optimized *AO* coronagraphs we describe here.

With an *AO* system in place, the image plane stop can be made very small: only slightly larger than the diffraction spot itself. However, a pupil plane stop matched to a reduced image plane stop must have a small clear diameter to significantly reduce the off-axis throughput; there is a trade-off between throughput and scattered light suppression. In some situations using a coronagraph does not improve the final dynamic range of an instrument — it simply extends the exposure time required for a given amount of detected signal.

To address this issue, we simulated image formation in a coronagraph mounted on a telescope with an *AO* system, and investigated the effects of atmospheric turbulence under a range of seeing conditions, telescope sizes, and *AO* system performance levels. We introduce the principles of coronagraphy with a simple one-dimensional model, and discuss the results of the simulations in the context of current and next-generation instruments.

Our model is an extension of that of Nakajima (1994), who modeled low order ground-based *AO* coronagraphs to determine the detectability of Jupiter-mass companions around main sequence stars. Nakajima simulated the *AO* wavefront correction by zeroing out the lowest order Zernike coefficients in the expression used to generate realizations of Kolmogorov-spectrum fluctuations in the atmosphere’s refractive index. In Nakajima’s work, the Lyot stop is “oversized” by a fixed amount (10%), and occulting stop sizes are chosen to be 1, 5, 10 and 15 times the telescope resolution. We extend Nakajima’s approach in four ways. First, we match the Lyot stop oversizing to the size of the image plane stop to optimize coronagraphic performance. Second, we use a graded high-pass filter to mimic *AO* correction. Third, we investigate higher order adaptive correction of the incoming wavefront to model *AO* systems with a few thousand actuators. We concentrate on the smallest stop sizes allowed by Fourier optics that do not lead to an unacceptable reduction in throughput. In earlier work (Makidon et al. 2000) we investigated occulting stop sizes between $3\lambda/D$ and $6\lambda/D$ radians. Here we present results for a single occulting image plane stop with a diameter of $4\lambda/D$ radians. Present-day computer memory and processor speeds, as well as the development of a rapid Markov algorithm to create the Kolmogorov-spectrum phase screens used to simulate atmospheric effects (Glindemann et al. 1993; Berkefeld et al. 2001b) enabled us to generate 1000 realizations of each instrument configuration. We therefore simulate long exposure

AO images which can be used to estimate detection limits, since speckle noise is often the limiting factor in faint companion detection (Racine et al. 1999; Marois et al. 2000).

2. Theory

To set the stage for discussion of a more realistic instrument, we illustrate the Fourier optics of a one-dimensional coronagraph. Other more formal expositions of coronagraphic imaging can be found in the literature (Noll 1976; Wang & Vaughan 1988; Malbet 1996). Our analysis assumes that the Fraunhofer approximation applies, *i.e.*, that the transverse electric field in the image plane is the Fourier transform of the phasor of the wavefront phase in the pupil plane (if $\phi(x, y)$ is the phase, then $e^{i\phi(x, y)}$ is the corresponding phasor). We make use of the standard Fourier analysis results which can be found in Bracewell (1986).

For this analysis we consider only monochromatic imaging, but note that in typical broad-band imaging, the final image can be described by the sum or integral of several monochromatic images, weighted by the instrumental transmission function. Wavelength variation across the band will act in such a way as to smear image features radially by the same factor as the fractional bandwidth, since the wavelength enters into diffraction-limited image formation only in the combination (λ/D) . As a result, bright Airy rings will get wider, but coronagraphic suppression of such rings will persist. By treating the monochromatic case we can distinguish clearly between halo suppression and Airy ring suppression. Secondary support spiders and scintillation (field strength variation) are not modeled here.

2.1. The one-dimensional coronagraph without an atmosphere

In the absence of atmospheric degradation, a monochromatic on-axis source at infinity produces a transverse electric field at the telescope pupil

$$E = E_0 \operatorname{Re}(e^{i(kz - \omega t)}), \quad (2-1)$$

where $k = 2\pi/\lambda$, the z axis is the optical axis, ω the angular frequency of the wave, t the time, and $\operatorname{Re}()$ denotes the real part of a complex number.

We follow the passage of the incident wave's field through a one-dimensional coronagraph. Figure 1 shows a diagram of the optical path.

We label eight key locations along this path with letters a–h. Eight plots in the figure show the electric field due to an on-axis source at these key locations, and the transmission functions of the optical stops that affect the incident wave as it passes through the coronagraph.

First, the incoming wave passes through the telescope aperture (Figure 1a). We represent this

interaction by multiplying the field by the aperture stop function, so that in the pupil plane

$$E_a = E \Pi(x/D_\lambda), \quad \text{where} \quad \begin{cases} \Pi(x) = 1 & \text{for } |x| < 1/2, \\ \Pi(x) = 0 & \text{elsewhere.} \end{cases} \quad (2-2)$$

Here $D_\lambda = D/\lambda$ is the number of wavelengths across the telescope aperture (which is also the inverse of the angular resolution of the telescope as measured in radians). We denote a pupil plane coordinate by x , and an image plane coordinate by θ . The telescope optics then form the wave into an image (Figure 1b). The electric field in the image plane is the Fourier transform of the aperture field E_a :

$$E_b \propto \text{sinc}(D_\lambda \theta), \quad (2-3)$$

where θ is the field angle in radians in the first image plane. We omit the constants of proportionality for simplicity.

In a conventional imaging camera this image field would fall on a detector here. However, in a coronagraph the star is occulted by a field stop in this image plane. We describe the stop in terms of a shape function $w(D_\lambda \theta/s)$, which is unity where the stop is opaque and zero where the stop is absent. If $w(\theta)$ has a width of order unity, the stop size will be of the order of s resolution elements. The transmission function in the image plane is therefore $1 - w(D_\lambda \theta/s)$ (Figure 1c). To illustrate the present discussion, we take $w(\theta) = \exp(-\theta^2/2)$. The field in the first imaging plane after the occulting stop (Figure 1d) can therefore be written as

$$E_d \propto \text{sinc}(D_\lambda \theta)(1 - w(D_\lambda \theta/s)). \quad (2-4)$$

This occulted image is relayed to a detector through a second pupil plane. The electric field at this second pupil is the Fourier transform of the occulted image field (see Figure 1e):

$$E_e \propto \Pi(x/D_\lambda) * (\delta(x) - \frac{s}{D_\lambda} W(sx/D_\lambda)) \quad (2-5)$$

Here W is the Fourier transform of the image stop function w , $\delta(x)$ is the Dirac delta function, and $*$ denotes convolution. W has width of order unity, although it will not have bounded support for occulting stop shape functions of finite extent, such as the hard-edged stop $w(\theta) = \Pi(\theta)$ (the support of a function is the set of points at which the function is non-zero). The geometrical significance of (2-5) becomes clear if we rewrite it as

$$E_e \propto \Pi(x/D_\lambda) - \frac{s}{D_\lambda} \Pi(x/D_\lambda) * W(sx). \quad (2-6)$$

If the image stop is completely opaque at its center, $w(0) = 1$. This means that its transform, $(s/D_\lambda) W(sx/D_\lambda)$, has unit area, regardless of any re-scaling of the argument of w . This makes for cancellation of the field across most of the pupil when $s \gg 1$. In Figure 2 we show how the

equation 2-6 is constructed graphically, using a Gaussian image stop whose width is $5\lambda/D$ (*i.e.* $s = 5$). This shows why the Lyot stop must mask out a border of order D/s wide around the pupil boundary to produce significant reduction in the throughput of unocculted light from the on-axis source. It is only at this stage that the coronagraph increases the dynamic range of the final image.

The unocculted light (Figure 1d) has a highly periodic distribution, with periodicity $\sim \lambda/D$. In the following pupil plane (which is the transform space of the image plane), this energy is concentrated near $\pm D/2$. The larger the occulting stop diameter, the more E_d looks like a pure sinusoid, and the more the unocculted energy is localized in the neighborhood of the boundary of the following pupil.

In seeing-limited coronagraphs, the occulting stop is typically many diffraction widths in size ($s \geq 10$). Consequently, the Lyot stop need only be undersized by a small fraction of the pupil diameter (*e.g.* 10% or less), resulting in minimal loss of throughput for unocculted, off-axis sources. In contrast, off-axis throughput in an optimized, diffraction-limited coronagraph with significant rejection of on-axis light must fall dramatically as the image plane stop shrinks to a few diffraction widths. This is because the spillover of unocculted on-axis light occurs in a wide border around the pupil boundary in the plane of the Lyot stop, so the Lyot stop must obscure a sizeable fraction of the re-imaged primary mirror to remove the on-axis spillover. Hence, off-axis throughput is reduced as well.

Since the scale of the Lyot stop oversizing is D/s , we fine-tune the Lyot stop diameter so that it obscures a border $\mathcal{F}D/s$ around the perimeter of the primary. The Lyot stop diameter is therefore

$$D_{Lyot} = D - 2\mathcal{F}D/s. \quad (2-7)$$

If a secondary obstruction is present, then the Lyot stop must block out a similar border around the inside edge of the annular pupil. This is why small secondary mirrors benefit diffraction-limited coronagraphy. In section 4.1 we describe how to choose an optimum value of \mathcal{F} for a given telescope and *AO* system under given atmospheric conditions.

Using the theory outlined above, in the the case of an unobstructed primary aperture with an image plane stop of $5\lambda/D$ (*i.e.*, $s = 5$), approximately 16/25 of the aperture should be obscured by a matched Lyot stop: when projected back onto the primary pupil, the Lyot stop is opaque outside a circle of diameter $\sim 3D/5$. Rejection of unwanted on-axis light must be balanced by signal-to-noise considerations pertaining to the off-axis source brightness. This places a practical lower limit on the angular size of the occulting spot in the first image plane.

The above arguments hold for two-dimensional apertures as well. The derivation is analogous to the one-dimensional case, although the functions and transforms become two-dimensional (*e.g.*, for a circular telescope aperture, the sinc function is replaced by the Airy function). Wang & Vaughan (1988) describe the two-dimensional case, and Malbet (1996) treats the *PSF*'s of off-axis sources in such coronagraphs.

2.2. The coronagraph in the presence of an atmosphere

In the absence of scintillation, we can model atmospheric effects on an incident plane wave by multiplying the aperture illumination function $\Pi(x)$ by an atmospheric disturbance phasor $e^{i\phi(x)}$. In our one-dimensional example, the resultant image field is the Fourier transform of $e^{i\phi(x)}\Pi(x/D_\lambda)$. For telescope diameters larger than $\sim 0.5\text{m}$ at wavelengths shorter than ~ 2 microns, the atmospheric phase function typically has significant power at length scales smaller than the aperture size, so a long exposure image under these circumstances exhibits the familiar unimodal seeing disk that is typical of images from large ground-based telescopes. In consequence, coronagraphs without *AO* systems on seeing-limited telescopes use occulting stops many diffraction widths wide, with concomitant high throughput as explained earlier. Stellar coronagraphy without adaptive wavefront correction, or with only tip-tilt systems, is still useful to prevent detector saturation, and has produced observations of considerable scientific value (Golimowski et al. 1992; Nakajima et al. 1995).

Ideally, a coronagraph with an *AO* system would be just like the coronagraph without an atmosphere. The image of a point source in the first image plane would be a pure Airy disk, and the size of the Lyot stop could be chosen using simple Fourier theory and a diagram like Figure 1. However, an *AO* system cannot correct atmospheric effects on spatial scales smaller than the inter-actuator spacing in the pupil plane. Power at high spatial frequencies that goes uncorrected in the pupil plane transforms into noise on large angular scales in the image plane. The corrected image consists of a diffraction limited core surrounded by an extended halo due to the uncorrected aberrations, a remnant of the uncorrected seeing-disk. The size and shape of the halo reflect the number of actuators in the *AO* system and the moment-to-moment characteristics of the turbulence in the atmosphere.

In the presence of this halo the choice of Lyot stop is not obvious. Indeed, a given *AO* configuration may not be able to reduce the power in the extended halo sufficiently to justify diffraction-limited coronagraphy — coronagraphy where the occulting mask is only a few diffraction widths across. In order to predict the size of the uncorrected halo and to understand how it affects coronagraphy, we modeled the effects of atmospheric turbulence on the incoming wavefront and the correction of these aberrations by *AO*. Our models allow us to find useful operating parameters for diffraction-limited coronagraphs working in concert with *AO* systems for a range of telescope sizes, *AO* capabilities, and observing conditions. Sections 4.1 and 4.2 discuss these issues in some detail.

3. Numerical Simulations

Each of our numerical simulations is characterized by the telescope entrance pupil size and geometry, the seeing, D/r_o , the number of actuators across the primary, N_{act} , the size of the occulting image plane stop, s , the Lyot stop fine tuning factor, \mathcal{F} , and the linear size of the array, N_s , sampling the incoming wavefront. We generate 1000 independent realizations of Kolmogorov-

spectrum phase screens in $2N_s$ by $2N_s$ arrays, with the spatial sampling of these arrays chosen to provide several samples across each Fried length r_o (Fried 1966), while constraining the sampling to force N_s to be a power of 2. Our resultant spatial sampling ranges from 3.2 to 21 samples across r_o (see Table 1).

We Fourier transform the input phase arrays, and multiply them by a high-pass filter to mimic the action of *AO*. Then we reverse-transform the filtered arrays to obtain the *AO*-corrected wavefront.

The shape of the *AO* filter near cutoff depends on details of the *AO* system. Deformable mirror (DM) actuator influence functions which extend to neighboring actuators' positions reduce the sharpness of the cutoff. Noisy wavefront sensing and intrinsic photon noise reduce the efficacy of high spatial frequency wavefront correction. The flow of the atmosphere past the telescope pupil and a non-isotropic refractive index spatio-temporal distribution also change the shape of the *AO* filter, as does imperfect DM calibration.

The cutoff frequency of the *AO* filter cannot be higher than the spatial Nyquist frequency of the actuator spacing, $k_{AO} = N_{act}/2D$. At a given wavelength λ , this spacing corresponds to an angle

$$\theta_{AO} = N_{act}\lambda/2D. \quad (3-1)$$

In earlier work (Makidon et al. 2000), our *AO* high-pass filter was the complement of a Hanning filter. This has a continuous derivative everywhere, and a very smooth approach to the cutoff. As we show in Section 5, this proved to be too conservative, as it underestimates the amount of observed *AO* correction. In these simulations we use a parabolic filter:

$$\begin{aligned} A(k) &= (k/k_{AO})^2 && \text{for } k < k_{AO} \\ A(k) &= 1 && \text{otherwise.} \end{aligned} \quad (3-2)$$

We show that this matches observed results over the range where comparison with data is valid.

To avoid edge effects introduced by the Fourier filtering, only the central N_s by N_s section of the filtered array is retained. This is then multiplied by a binary mask representing the telescope entrance pupil. This mask is opaque (zero) outside the primary mirror edge, and inside the secondary obstruction. Secondary support spiders, mirror surface micro-roughness and scattering are not considered in these simulations.

We embed the filtered and masked array in the center of an $8N_s$ by $8N_s$ zero-filled array. This results in image field sampling of $\lambda/8D$. which allows for effective comparison with data taken with $\sim \lambda/4D$ pixels.

We then create the complex phasor $e^{i\phi(x,y)}$ describing the electric field corresponding to the phase $\phi(x,y)$, and Fourier transform the phasor to obtain the first image field. We average all 1000 realizations of the intensity of this image, as well as the Strehl ratios derived from these images as a measure the *AO* system performance.

This *AO*-corrected image field is then multiplied by another binary mask to produce the effect of the image plane stop, and the product is inverse-transformed to create the pupil field at the Lyot plane, where it is multiplied by a third binary mask representing the Lyot stop. The final image is produced by Fourier transforming this field. We average all realizations of the final image intensity, along with the values of various throughput and geometrical obstruction descriptors of the optical system. These averaged images can be thought of as a single image with an exposure time corresponding to a thousand times the speckle lifetime. This is equivalent to a ~ 100 second exposure at Palomar in the *K*-band.

4. Optimizing Coronagraph Design

In this section we present the results of numerical investigations into when *AO* benefits coronagraphy, and how one optimizes the design parameters for a coronagraph used in conjunction with an *AO* system.

4.1. Optimizing the Lyot Stop

In section 2 we defined the diameter of the Lyot stop as $D - 2\mathcal{F}D/s$, where \mathcal{F} is the Lyot stop fine tuning factor. Here we show how the value of \mathcal{F} is chosen to optimize a coronagraph for a specific telescope under particular atmospheric conditions. We present the results of an exploration of a coronagraph on the Gemini telescope with atmospheric turbulence described by $D/r_o = 30$.

The uppermost curve in Figure 3a shows an azimuthally averaged PSF that an *AO* system with 51 actuators across the primary diameter (a total of 2042 actuators) delivers. A hundred independent atmospheric phase disturbance realizations have been averaged into this PSF, which is normalized to unity at its center. The Strehl ratio of the corresponding image is 82%.

Below this we show azimuthally averaged PSF's of a coronagraph with a central stop of $4\lambda/D$ diameter, with three different values of \mathcal{F} . These curves have been re-normalized to take into account the dimming of the image due to throughput losses that result from undersizing the Lyot stop. This is accomplished by dividing the simulated profile by the Lyot stop clear fraction (the ratio of the clear area of the Lyot stop, when projected back to the primary, to the clear area of the entrance pupil). If the *AO*-corrected PSF and a coronagraphic PSF coincide at some particular value of the radial distance from the central object, then, at that separation there is no dynamic range gain to be had from using that coronagraph. At such a location the same companion signal-to-noise ratio will be achieved when the same number of source photons have been detected. In this case the coronagraphic configuration simply increases the exposure time required to achieve the same signal-to-noise ratio, because it is equivalent to using a telescope with a smaller collecting area.

Figure 3b shows the ratios of the various renormalized, azimuthally averaged coronagraphic PSF’s to the PSF with just the *AO* system and no coronagraph. Three values of the fine tuning parameter \mathcal{F} are presented: 0.25, 0.5 and 0.75. The PSF for least aggressive Lyot stop ($\mathcal{F} = 0.25$) shows the least dynamic range benefit. Bright re-imaged pupil edges are not sufficiently masked out, though the Lyot stop is 72% clear. The most aggressive stop ($\mathcal{F} = 0.75$) masks out much more of the bright pupil edges, but the Lyot stop is only 20% clear. This results in a drastic reduction in the brightness of off-axis sources. The intermediate Lyot stop ($\mathcal{F} = 0.5$) does a better job of balancing the obscuring of bright pupil edges, and has a Lyot stop throughput of Lyot stop (43%). For a specific instrument project this optimization will need to be done on broad-band images, with finer resolution in the \mathcal{F} parameter space. We present this coarse optimization search as a model for further work tailored to particular telescopes and science drivers.

4.2. Threshold AO performance for coronagraphy

Here we consider the transition between seeing-limited and high Strehl imaging. We select fixed seeing conditions ($D/r_o = 30$), and vary the actuator spacing of the *AO* system. The resulting images have Strehl ratios between 30% and 90% as the number of actuators across the primary diameter goes from 26 to 71 (Figure 4). The validity of our *AO* correction algorithm is discussed in section 5, we merely note here that it is based on real data. We normalize the PSFs in Figure 4 to be unity at the center because we wish to present dynamic range gains rather than absolute flux levels.

The PSF is described by a diffraction-limited core, a flat *AO*-corrected halo out to a shoulder at a radius θ_{AO} where the *AO* stops working. After that the profile shows the familiar atmospheric wings. The flat plateau of *AO* correction drops in intensity and grows in radius as the number of actuators increases. It is the uncorrected light in this area that is redistributed into Airy rings by the *AO* system, and it is this light that is not removed by a coronagraph. The image with a Strehl ratio of 30% has a ten-fold decrease in the intensity of this scattered light as compared with the 53% Strehl image. This demonstrates why there is a threshold Strehl required for coronagraphic imaging targeted at a particular angular distance from the central source.

Azimuthally averaged PSF’s (dotted lines) for the same 100 realizations of the atmospheric phase disturbances corrected by *AO* systems with a range of actuator spacings are shown in Figures 5a – 5f. Below these PSF’s we plot renormalized PSF’s for a coronagraph with a $4\lambda/D$ occulting spot and a Lyot stop fine-tuning parameter of $\mathcal{F} = 0.5$. The vertical scales on all these plots is the same, and the PSF is normalized to unity at the origin.

The effect of increased *AO* correction on direct imaging is manifest in the steadily decreasing intensity of the wings relative to the central peak.

At a Strehl ratio of 53% (Figure 5a), the wings of both the direct and coronagraphic PSF’s are about 10^{-3} of the central intensity. There is little suppression of the halo of the image, though

bright Airy rings are removed out to a radial distance of $\sim 6\lambda/D$. Scattered light from uncorrected atmospheric aberrations are not suppressed by the coronagraph. At a Strehl ratio of 62% (Figure 5b), AO correction produces visible Airy rings further out, since more light is guided into the Airy pattern and less light is scattered semi-randomly into the halo. Again, residual scattered light is not suppressed coronagraphically, and it still limits dynamic range. In Figures 5c and 5d we see further reduction in the scattered light halo, and a corresponding increase of energy in the pure Airy pattern. Coronagraphic imaging suppresses the image to well below the darkest Airy rings, a phenomenon we call halo suppression, since that is how it appears to the observer, even though it is really suppression of a coherent diffraction pattern emerging because of the reduction in halo intensity.

By the time the Strehl ratio has risen to 82% (Figure 5d), an annulus of greatly increased dynamic range opens up between the occulting stop edge at a radius of $2\lambda/D$, and the radius at which the remaining halo is comparable in intensity to the Airy pattern, at a radius of $4\lambda/D$. It is in such regimes that dynamic range increases dramatically. Below such Strehl ratios a coronagraphic spot with a $4\lambda/D$ diameter would not produce much gain in dynamic range.

The improved dynamic range would continue indefinitely if AO guide stars were bright enough. However, for a given primary area, as the number of AO channels increases, the number of photons per channel available to use for AO correction decreases. We extrapolate from Palomar AO system performance to the regimes shown in Figures 5e and 5f as goals that could be reached by the next generation of AO systems on 8m telescopes at good astronomical sites.

5. Comparison of Simulations with Palomar PHARO Observations

We compared our monochromatic models to a 180 second *K*-band exposure obtained with the PHARO camera on the Palomar AO system, using an image plane stop of $0''.96$ in diameter (Oppenheimer et al. 2000). We used the appropriate Lyot oversizing to match the PHARO coronagraphic Lyot stop dimensions ($\mathcal{F} = 1.07$, or a clear aperture of 4m), and match the AO system actuator spacing of 16 across the primary. Details of the PHARO camera optics are described in Hayward et al. (2000).

Figure 6 shows an overlay of the radial profiles of our simulations with $D/r_o = 10$ and the parabolic AO high pass filter (dashed), against the data (solid). Both images were normalized to contain unity power out to a radius of $4''0$.

Our choice of D/r_o results in a match with the wings of the stellar image past $\theta_{AO} = 8\lambda/D$ (where the AO ceases to improve the image). We did not need to fine-tune the Fried length r_o to match the observing conditions when the data were taken, as our initial guess at r_o provided a sufficiently accurate estimate of the azimuthally averaged stellar wing profile. Other effects (non-Kolmogorov spectra, instrumental scatter, the effects of the secondary support spiders, waffle or other wavefront reconstructor errors, *etc.*) could also be present in the PHARO data.

The simulated image plane stop has a diameter of $10.6\lambda/D$ at 2.2 microns. Therefore the region where our model is tested by the data lies between $5.3\lambda/D$ ($0''.48$) and $\theta_{AO} = 8\lambda/D$ ($0''.73$). Our model differs from observations by a few percent over the entire range where the comparison is valid. Detailed work on matching simulations with this data will be presented elsewhere (Sivaramakrishnan and Oppenheimer 2001).

The comparison with data suggests that our representation of *AO* correction as a parabolic filter is accurate enough to be used to predict system performance of the next generation of *AO* coronagraphs.

6. DISCUSSION

In order to span a range of telescope sizes, we simulated the KPNO Calypso 1.2m, the Palomar Hale 5m, and the Gemini 8.1m. We reproduce the secondary obscuration ratios of each telescope, though we do not model secondary support spiders.

Atmospheric phase screen realizations using one or a few representative values of the Fried length relevant to the sites are input to the optical train simulation after being smoothed by the *AO* filter. The effect of wind on the delivered Strehl ratio have not been incorporated.

We match the *AO* system actuator density on the primary apertures to those presented in previous work (Makidon et al. 2000). A summary of the relevant input parameters (primary and secondary mirror diameters, number of actuators, and input D/r_0 values) can be found in Table 1.

While we examined a variety of image plane occulting stop sizes, we only present one stop size, $4\lambda/D$, in this paper. Our choice of this stop diameter is based on previous work which suggests $4\lambda/D$ is close to the smallest effective stop size for imaging stellar coronagraphs with Strehl ratios between 70% and 95% (Makidon et al. 2000). Larger stops simply obscure more of the improved image without a significant increase in the dynamic range of the final images. We find that stops smaller than $4\lambda/D$ require extreme oversizing of the Lyot stop, dramatically reducing system throughput. We note that for larger values of the image plane stop diameter, the Lyot throughput penalty is reduced. In consequence, the optimal value of \mathcal{F} is expected to grow with increasing values of s when $s \lesssim 10$.

Two values of \mathcal{F} , 0.5 and 0.25, are examined here. These yield Lyot stop outer diameters of $0.75D$ and $0.875D$ respectively for our image plane stop. The effect of the two Lyot stops on the final image are illustrated in the *PSF* plots of Figures 7, 8 and 9. In general, we find a coronagraph coupled to the more aggressive Lyot stop ($\mathcal{F} = 0.5$) is significantly better at suppressing both Airy ring and halo contributions to azimuthally averaged *PSFs* than the higher throughput one ($\mathcal{F} = 0.25$).

The coronagraphic *PSF*'s presented in Figures 7, 8, and 9 take into account the Lyot stop throughput losses, as they have been renormalized by dividing by the ratio of the Lyot stop area to

the primary aperture area. When the image profiles with and without the coronagraph coincide, no gain in dynamic range is attained by using a coronagraph.

We indicate the stop edge in these figures with a vertical line. We also mark where the *AO* stops working (at the angular distance θ_{AO}) with a triangular symbol if this occurs within the plot boundaries. In our Gemini simulations *AO* this angle falls outside the borders of the *PSF* plots.

6.1. Kitt Peak Calypso 1.2m telescope

The Kitt Peak Calypso 1.2m telescope was designed and constructed to minimize the deleterious effects of ground-level turbulence and scattered light on astronomical observations (Smith 1999). This telescope’s instrumentation operates in optical bandpasses.

For a small-aperture telescope like Calypso, we found that Strehl ratios of at least 60% are necessary for useful *AO* coronagraphy. The simulation we present has a 75% Strehl ratio. Smith (1999) reports upper quartile r_o ’s of 20cm or less in the *V* band at this site — we use a value of 24cm.

The Airy rings are well-suppressed out to many diffraction widths when $\mathcal{F} = 0.5$ (Figure 7a). The broad underlying halo is reduced by about a factor of three a few resolution elements past the image plane stop with this Lyot stop.

6.2. Palomar Hale 5m telescope

The Hale 5m has a functioning 241-channel *AO* system with a dedicated near-infrared science camera, PHARO (Hayward et al. 2000), which contains a variety of coronagraphic image plane and Lyot stops.

When $D/r_0 = 10$ we expect Strehl ratios of the order of 80% (Figures 8a and 8b). Such conditions can be expected in the *K*-band on good nights. At this Strehl ratio the Airy ring structure is almost completely removed, and halo is reduced by about a factor of two between the stop edge at $2\lambda/D$ and $\sim 5\lambda/D$ when $\mathcal{F} = 0.5$ (Figure 8b). The benefits of using a coronagraph when the *AO* delivers a 50% Strehl ratio are greatly diminished, as can be seen by comparing figures 8b and 8d. Thus the current 241-channel Palomar *AO* system is suited to *K*-band coronagraphy under good conditions. A system upgrade to *e.g.*, twice the number of actuators will enable the coronagraph to open up a larger search annulus in the *K*-band, and produce useful dynamic range gains in the *H*-band. To exploit the full potential of coronagraphic imaging on this system, upgraded wavefront reconstruction may be needed to delve into the cores of the images at angular separations of the order of the stop radius of $2\lambda/D$ from the target *AO* star.

6.3. Gemini 8.1m telescope

Gemini has a near-infrared coronagraph under construction, and will be equipped with a low order AO system, which enables high order second stage AO (Angel 1992) to be incorporated into a dedicated AO coronagraph. We used values of the Fried length which apply in the near-infrared. Under these conditions, expected Strehl ratios of 80% – 95% produce extremely effective coronagraphic suppression. In addition, $\theta_{AO} = 25\lambda/D$, so the annulus of high dynamic range imaging is relatively large (Figure 9a through 9f).

With $D/r_o = 30$, image halo reduction by a factor of three is observed a few diffraction widths outside the stop edge, and Airy ring suppression by another factor of three extends out to $\sim 5\lambda/D$ (Figure 9f).

At the other extreme, when $D/r_o = 15$ (*e.g.*, in the K -band), performance improves dramatically — in Figure 9b we see Airy ring suppression of a factor of over 10 or more in the bright rings located at 3.5 and 5.5 λ/D , and halo suppression of three out to $\sim 7\lambda/D$.

In Figures 10a – 10d we show simulated images for companions with brightness differences Δm of +5, +7.5 and +10 magnitudes relative to the on-axis target. In the absence of noise, we see that a companion with $\Delta m = +10$ at a separation of $0''.16$ is observable in the H -band under good seeing conditions ($D/r_o = 15$) with a 2000 channel AO coronagraph with a $0''.16$ diameter field stop (Figure 10d). The exposure time corresponding to these simulated images is ~ 1000 speckle lifetimes.

7. Conclusion

Diffraction-limited AO coronagraphy targets an entirely different search space from seeing-limited coronagraphs. Traditional coronagraphy under seeing-limited conditions provides image suppression where the seeing halo drops below the Airy pattern’s wings (Macintosh 2000). Typically this is tens of diffraction widths away from the central bright object. The advantage of diffraction-limited coronagraphic imaging is concentrated in an annulus starting just outside the image stop, and ending where the AO system stops improving the wings of the AO target star’s image. The size of the outer edge of this annulus is set by observing wavelength and the spatial Nyquist frequency of the AO system actuators when projected on to the primary. When small image plane stops are used the Lyot stop size must be carefully chosen to find the best trade-off between throughput and image suppression. Coronagraphic instruments might work extremely well in the near-infrared and longer optical bandpasses on large telescopes with the next generation of deformable mirrors using a few thousand actuators, provided wavefront correction is done well.

For 1-m class telescopes at $1\mu\text{m}$, we find that AO systems can deliver Strehl ratios $\geq 60\%$ without excessively compromising the brightness limits of available AO . However, only modest contrast ratio gains are achieved with a coronagraph on such telescopes. Coronagraphic suppression

is evident mostly in the bright Airy rings of the image.

The existing 241-actuator Palomar *AO* system is useful for *K*-band coronagraphy. Stop sizes down to at least $4\lambda/D$ are theoretically possible. Improved wavefront reconstruction may be necessary for these small occulting stops. With double the number of *AO* channels and reduced wavefront sensor read noise, this telescope could deliver Strehl ratios of 90% at $2.2\mu\text{m}$. *H*- and *K*-band coronagraphy would then become more scientifically profitable because of the increased dynamic range in this search space.

On 8-m class telescopes, tremendous coronagraphic gains are to be had with 2000 channel *AO* systems. With occulting stop diameters of $\sim 0''.15$, three-fold halo suppression and ten-fold bright ring suppression can be expected a few diffraction widths from the stop edge. Such a system on the Gemini telescopes would be ideally suited to high dynamic range coronagraphy in the *H*-band, with limiting Strehl ratios of $\sim 90\%$ possible around an M0 dwarf *AO* target ~ 20 parsecs away.

We thank B. Brandl and S. R. Kulkarni for posing questions that led to this investigation, and P. E. Hodge, T. Nakajima, B. A. Macintosh, and B. R. Oppenheimer for insightful discussions. B. R. Oppenheimer also provided us with pre-publication data. We are indebted to J. P. Lloyd for a critical reading of our simulation code, and the anonymous referee for helpful suggestions. We also thank R. J. Allen, J. R. Graham, E. P. Nelan, and R. L. White for encouraging the investigation. This work was funded in part by grants from the STScI Director's Discretionary Research Fund to AS and RBM, and the STScI Research Programs Office and visitors program for travel support for AS and CDK.

REFERENCES

- Angel, J. R. 1994 *Nature*, 368, 203
- Berkefeld, T., Glindemann, A. & Hippler, S. 2001, in preparation
- Berkefeld, T., Weiss, R. & Glindemann, 2001, in preparation
- Bracewell, R. N. 1986, *The Fourier Transform and its Applications* (McGraw Hill; London)
- Fried, D. L. 1966, *JOSA*, 56, 1372
- Glindemann, A., Lane, R. G. & Dainty, J. C. 1993, *Journal of Modern Optics*, 40, 2381
- Golimowski, D. A., Clampin, M., Durrance, S. T., & Barkhouser, R. H. 1992, *Appl. Opt.*, 31, 4405
- Guyon, O., Roddier, C., Graves, J. E., Roddier, F., Cuevas, S., Espejo, C., Gonzales, S., Martinez, A., Bisiacchi, G. & Vuntmeri, V. 1999, *PASP*, 111, 1321
- Hayward, T. L., Brandl, B., Pirger, B., Blacken, C., Gull, G. E., Schoenwald, J. & Houck, J. R. 2000 *PASP*, in press
- Lyot, B. 1939 *MNRAS*, 99, 580
- Macintosh, B. A. 2000 private communication
- Makidon, R. B., Sivaramakrishnan, A., Koresko, C. D., Berkefeld, T., Kuchner, M. J. and Winsor, R. 2000, in *Adaptive Optical Systems Technologies*, P.L. Wizinowich, ed. Proceedings of SPIE, Vol. 4007, ppp
- Malbet, F. 1996, *A&A*, 115, 161
- Marois, C., Doyon, R., Racine, R. & Nadeau, D. 2000, *PASP*, 112, 91
- Nakajima, T. 1994, *ApJ*, 425, 348
- Nakajima, T., Oppenheimer, B. R., Kulkarni, S. R., Golimowski, D. A., Matthews, K., & Durrance, S. T. 1995, *Nature*, 378, 463
- Noll, R. J. 1976, *JOSA*, 63, 1399
- Oppenheimer, B. R., Dekany, R. G., Hayward, T. L., Brandl, B., Troy, M. and Bloemhof, E. E. 2000, in *Adaptive Optical Systems Technologies*, P.L. Wizinowich, ed. Proceedings of SPIE, Vol. 4007, ppp
- Racine, R., Walker, G. H., Nadeau, D., Doyon, R. & Marois, C. 1999, *PASP*, 111, 587
- Sivaramakrishnan, A. & Oppenheimer, B. R. 2001 in preparation

Smith, E. 1999, Ph. D. thesis, Columbia University

Wang, T. & Vaughan, A. H. 1988, *Appl. Opt.*, 27, 27

Table 1. Properties of Telescope Simulations

Telescope	D	D_s/D	N_{act}	N_{chan}	N_s	D/r_0	Strehl (%)
Calypso	1.2	0.36	7	38	64	5.0	75
Palomar	5.08	0.33	16	201	64	10.0	79
						20.0	48
Gemini	8.1	0.13	51	2042	128	15.0	94
						22.5	89
						30.0	80

Note. — For this table, D and D_s are the primary and secondary mirror diameters (in meters). N_{act} is the number of actuators across primary mirror diameter, N_{chan} the estimated number of *AO* channels within the pupil, and N_s the number of wavefront phase samples across the primary mirror diameter.

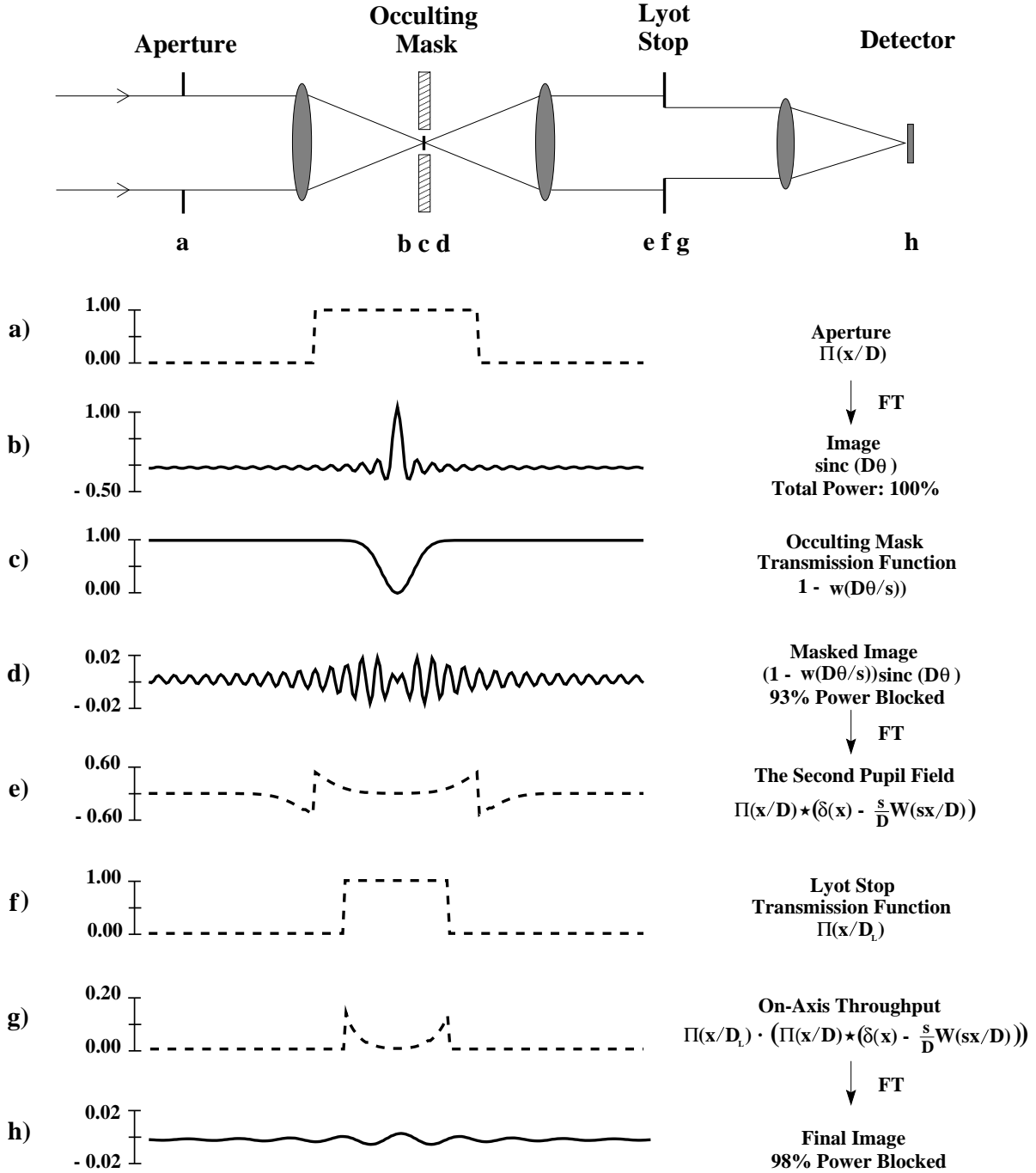


Fig. 1.— One-dimensional coronagraph summary, with locations and electric field or stop profiles of: (a) primary pupil for on-axis source; (b) image before image plane stop; (c) image plane stop; (d) image after image plane stop; (e) pupil before Lyot stop; (f) Lyot stop; (g) pupil after Lyot stop; and (h) final on-axis image. In this example, 98% of the incident power is blocked by the coronagraph.

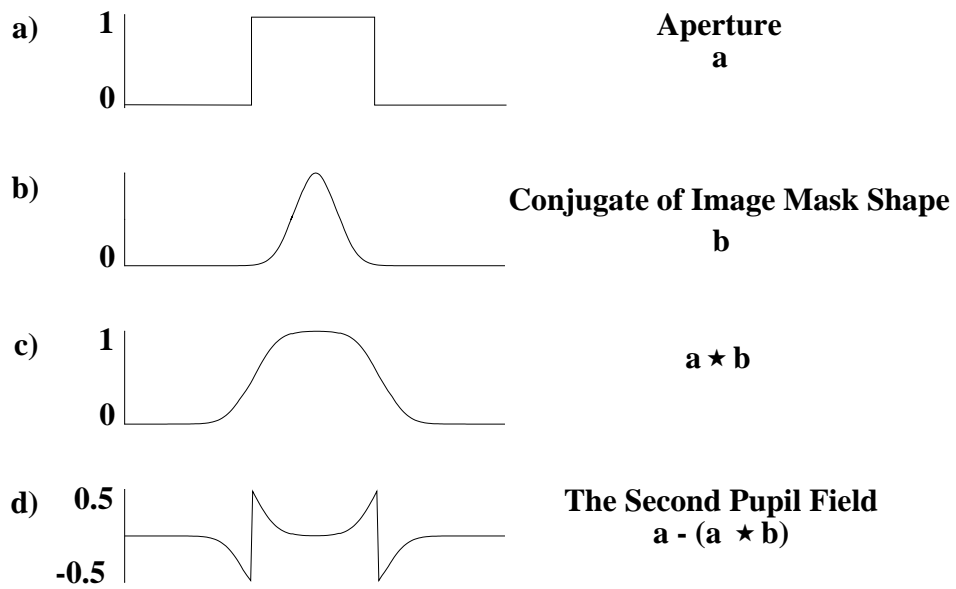


Fig. 2.— Graphical representation of the Lyot plane electric field calculation: (a) pupil function of width D ; (b) Gaussian profile image plane stop with $5\lambda/D$ standard deviation produces a Gaussian with standard deviation $D/5$ in the Lyot plane; (c) the convolution of the pupil function with the transform of the stop profile; (d) the final Lyot stop field showing bright edges and no energy in the center.

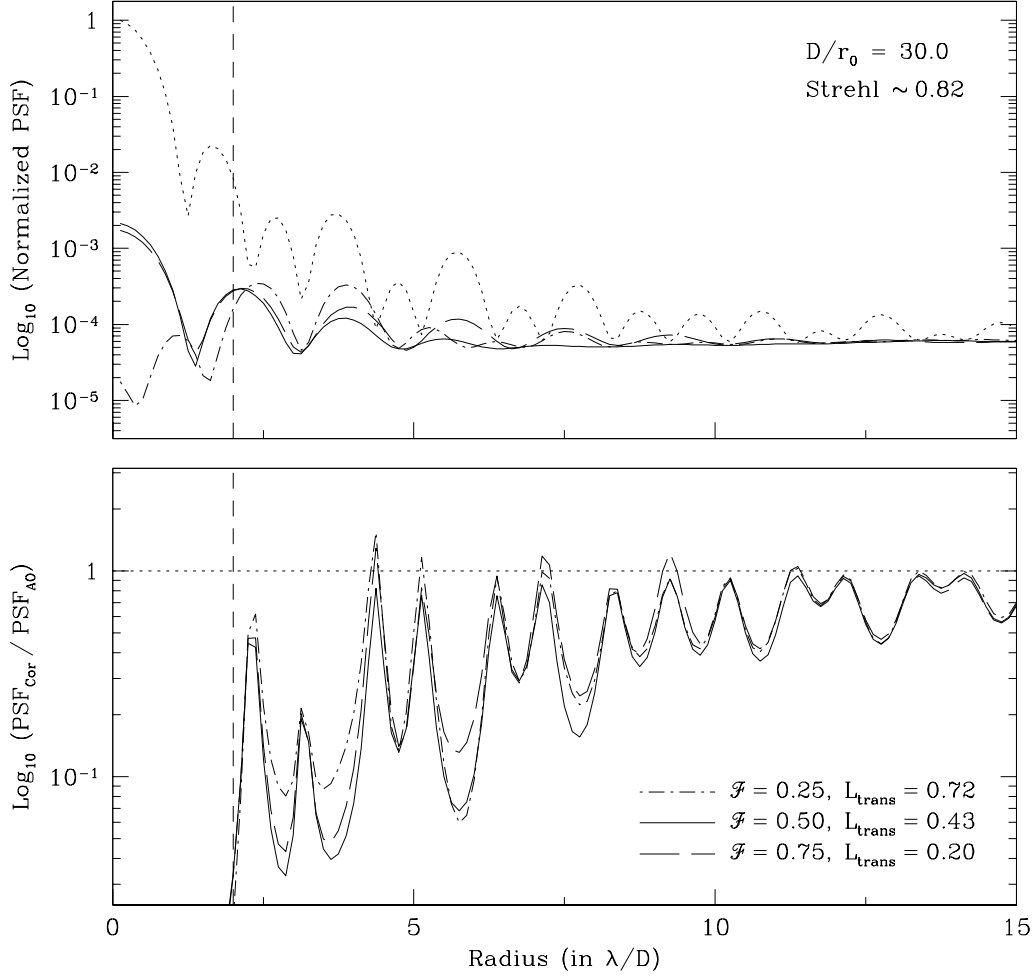


Fig. 3.— Optimizing the Lyot stop diameter. Top panel: azimuthally averaged *AO*-only PSF (dotted line), and three coronagraphic PSF’s with different Lyot stop diameters. The coronagraphic PSF’s have been re-normalized to take Lyot stop losses into account (see text). A $4\lambda/D$ angular diameter occulting image plane stop, whose edge is indicated by a dashed vertical line in both panels, is used in these coronagraphic simulations. Three values of the Lyot stop fine tuning parameter \mathcal{F} describing the Lyot stop size are presented. Bottom panel: ratios of the azimuthally averaged coronagraphic PSF’s to the *AO*-only PSF. The most effective central image suppression is seen over a few diffraction rings outside the image plane stop for the intermediate value of \mathcal{F} .

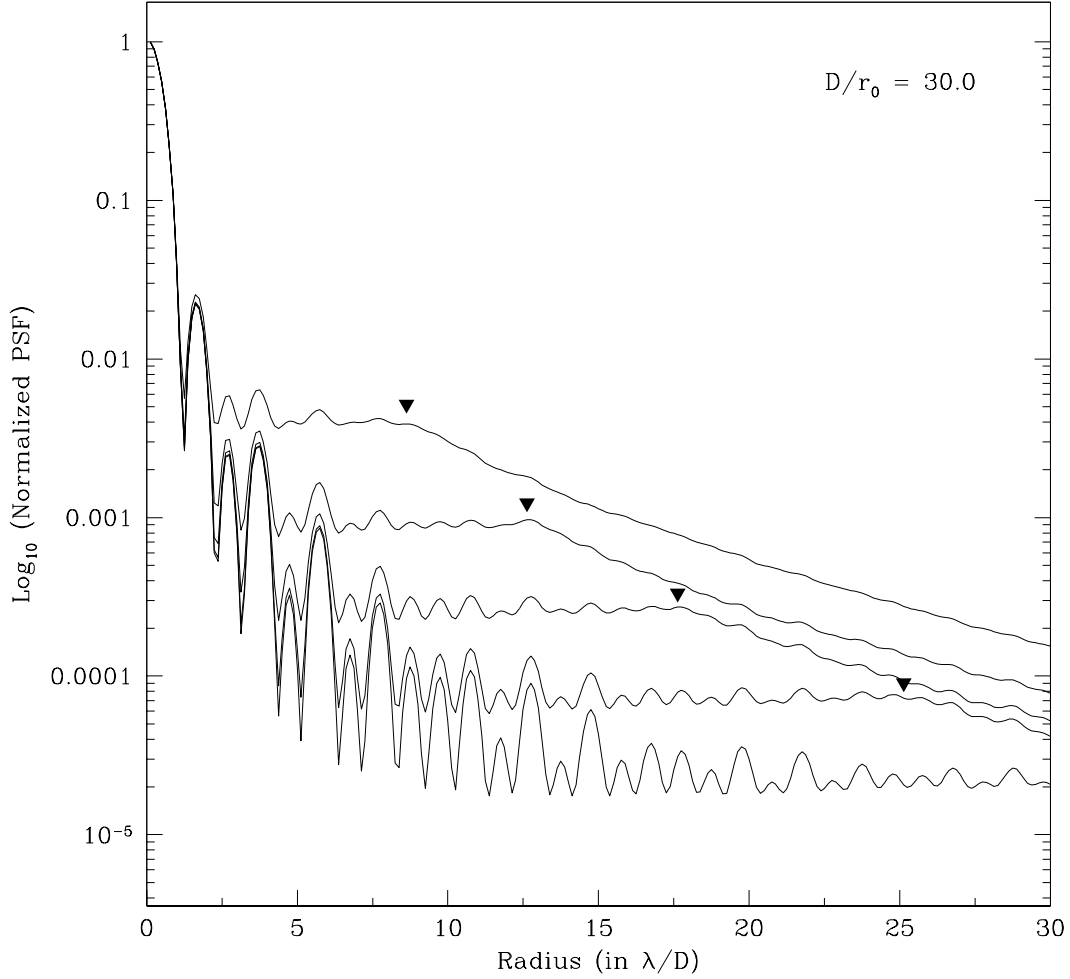


Fig. 4.— The effect of increasing AO correction is seen here. The same 100 independent realizations of a Kolmogorov-spectrum phase screen representing atmospheric wavefront aberration corrected by AO systems with 18, 26, 36, 51 and 71 actuators across a $D = 8.1\text{m}$ primary mirror, with $D/r_o = 30$. The azimuthally averaged PSF's are normalized to unity at their center. The Strehl ratios are 0.30, 0.53, 0.69, 0.82 and 0.90 respectively. Note the widening plateaus of partial correction extending to the shoulder (solid triangle) at a distance of θ_{AO} from the center of the image. Outside this plateau AO correction does not improve the image.

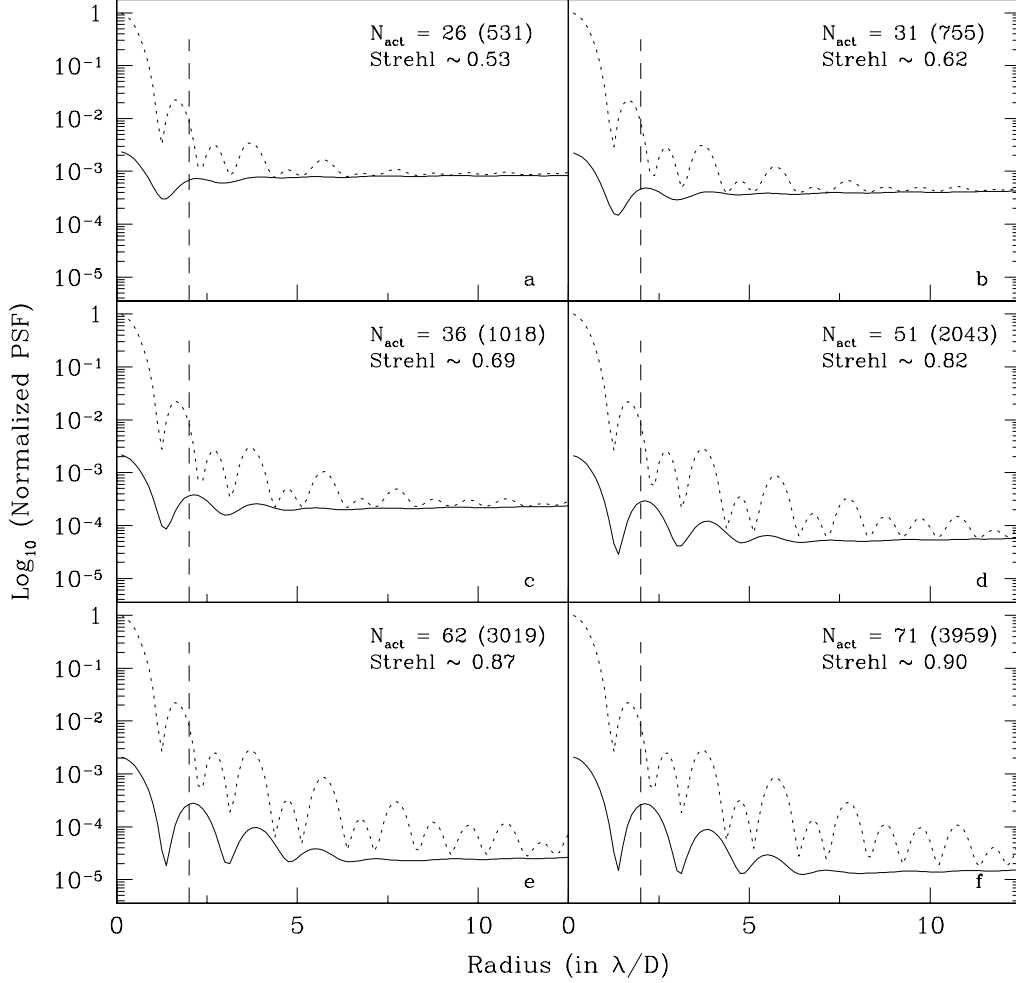


Fig. 5.— The effect of varying degrees of *AO* correction on increased dynamic range produced by a coronagraph with a $4\lambda/D$ occulting stop diameter. The dotted lines are azimuthally averaged, co-added PSF’s for the same 100 realizations of Kolmogorov-spectrum atmospheric phase disturbances with $D/r_o = 30$. Solid lines are renormalized azimuthally averaged co-added PSF’s of the same atmospheric phase realizations using a coronagraph with a Lyot stop fine-tuning parameter of $\mathcal{F} = 0.5$. The vertical scales are identical, and the non-coronagraphic PSF’s are normalized to unity at the origin. Renormalization is performed by dividing coronagraphic PSF’s by the fractional throughput of the corresponding Lyot stops (see text). Panels a through f show the emergence of an annulus of image suppression outside the occulting stop edge as the Strehl ratio increases from 53% to 90%.

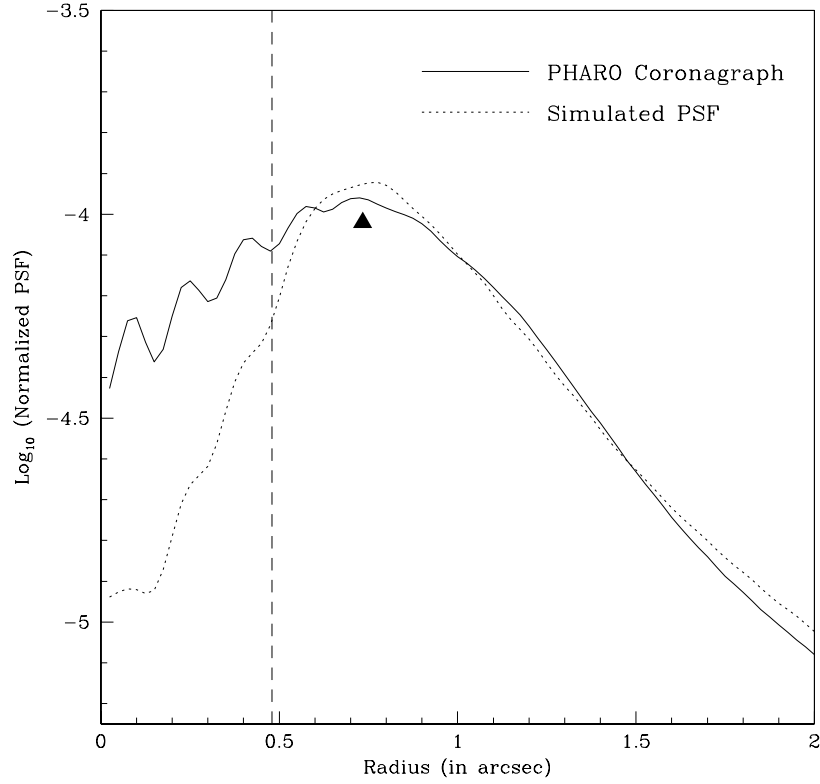


Fig. 6.— Azimuthally averaged image profiles of observed PHARO K -band data (solid) and our simulations with $D/r_o = 10$, and a parabolic AO high pass filter (dashed). Both images were normalized to contain unity power out to $4''$.

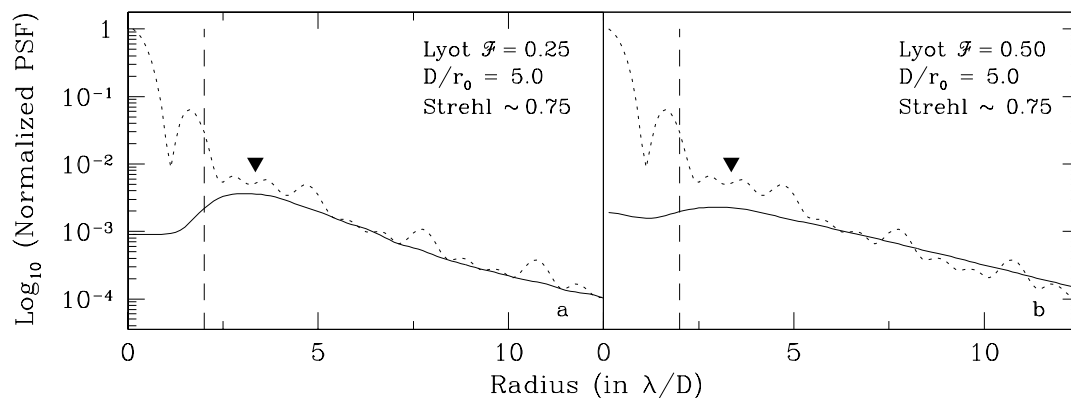


Fig. 7.— Azimuthally averaged *PSF*'s for the 1.2m Calypso telescope, with 7 actuators across the pupil diameter (~ 38 actuators within the pupil) and an occulting image stop of $4\lambda/D$. ($0''.48$ at $\lambda = 0.7\mu\text{m}$). The Lyot stop fine tuning parameter \mathcal{F} is 0.25 on the left, and 0.5 on the right (see text). The solid line shows the *AO*-corrected *PSF*, the dashed line shows the image profile after the coronagraph.

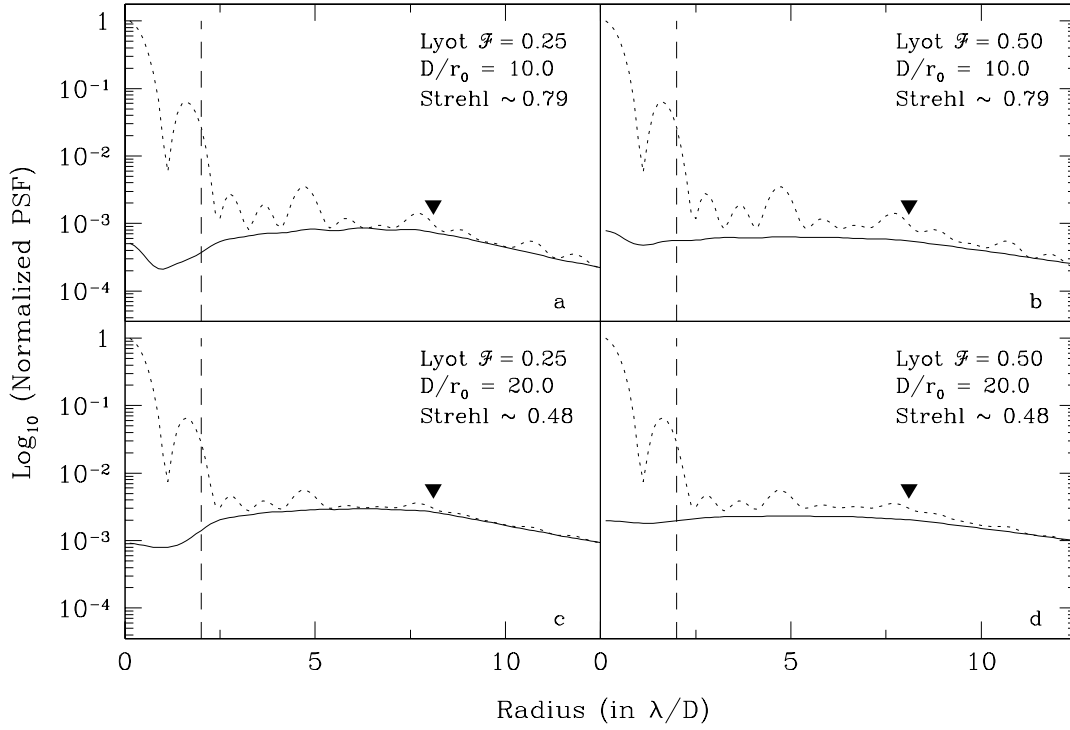


Fig. 8.— Azimuthally averaged *PSF*'s for the 5m Palomar Hale telescope, with 16 actuators across the pupil diameter (~ 216 actuators within the pupil) and an occulting image stop of $4\lambda/D$ ($0''.27$ at $\lambda = 2.2\mu\text{m}$). The Lyot stop fine tuning parameter \mathcal{F} is 0.25 on the left, and 0.5 on the right (see text). The solid line shows the *AO*-corrected *PSF*, the dashed line shows the image profile after the coronagraph.

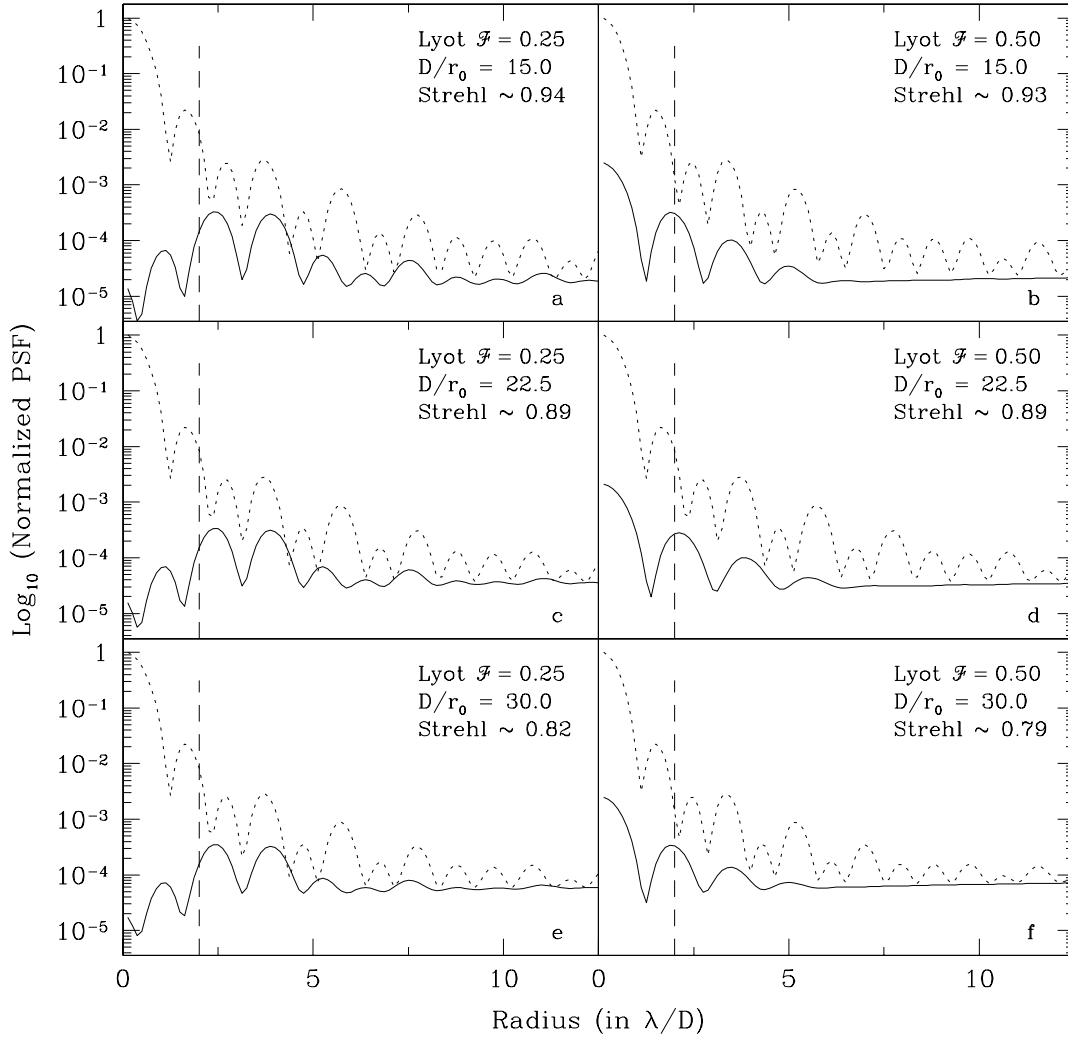


Fig. 9.— Azimuthally averaged *PSF*'s for the 8.1m Gemini telescope, with 51 actuators across the pupil diameter (~ 2042 actuators within the pupil) and an occulting image stop of $4\lambda/D$ ($0''.16$ at $\lambda = 1.6\mu\text{m}$). The Lyot stop fine tuning parameter \mathcal{F} is 0.25 on the left, and 0.5 on the right (see text). The solid line shows the *AO*-corrected *PSF*, the dashed line shows the image profile after the coronagraph.

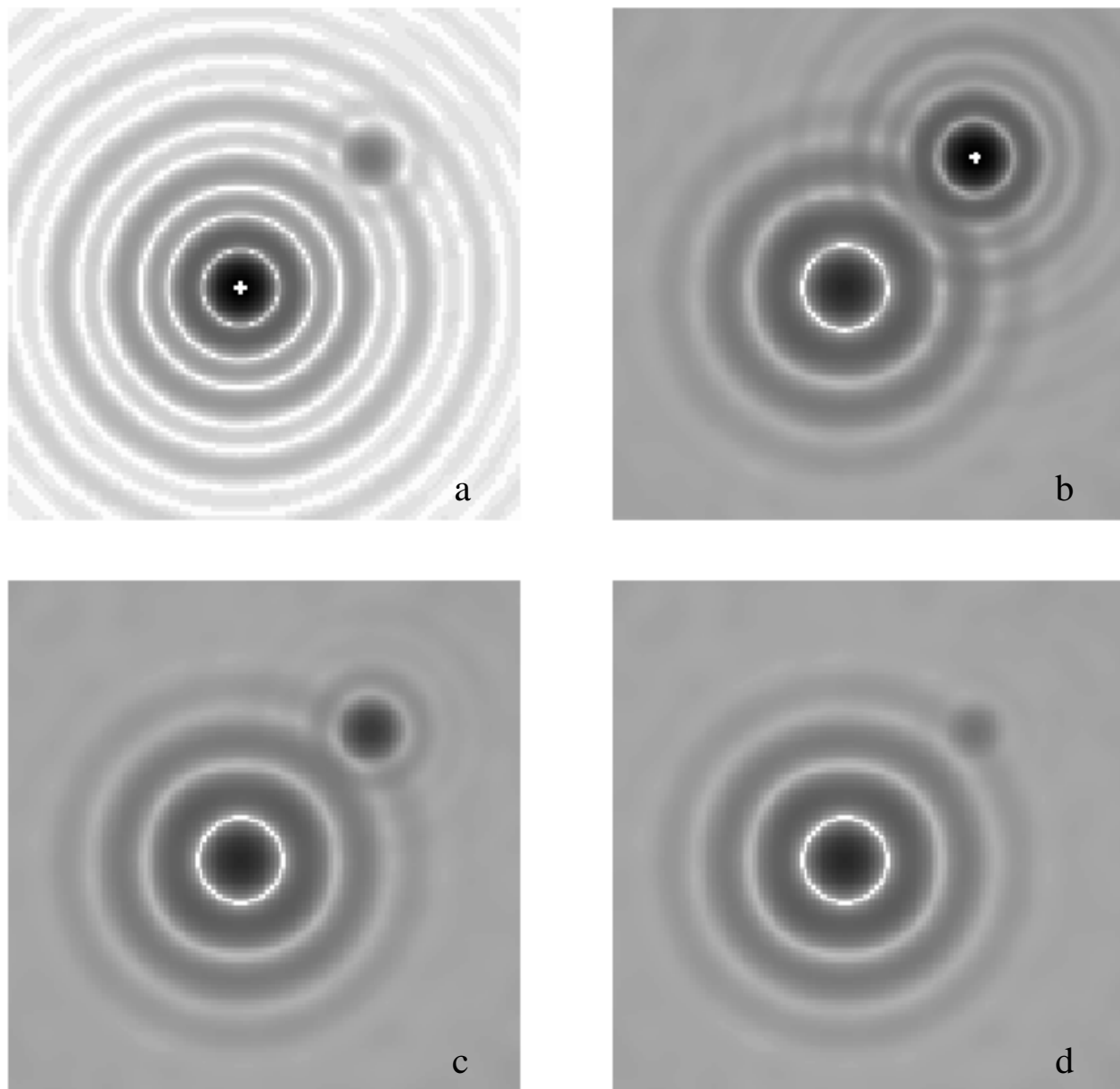


Fig. 10.— Realizations of a star with a faint companion at $4\lambda/D$ separation with $D/r_o = 15$ for the Gemini 8.1m telescope assuming 2042 channels of *AO*. In (a) we show the primary star and a companion of $\Delta m = +5$ with no coronagraph in place. Figures (b), (c) and (d) exhibit companions of $\Delta m = +5$, $+7.5$ and $+10$ magnitudes respectively, with the primary occulted by an image plane stop of diameter $4\lambda/D$ ($0''.16$ in the *H*-band).